Polarization and CEP dependence of the transverse phase space in laser driven accelerators

A. Seidel,[1,2,*] B. Lei,[1,2,3,†] C. Zepter,[1,2] M. C. Kaluza,[1,2,3] A. Sävert,[1,2,3] M. Zepf,[1,2,3] and D. Seipt[2,3]

[1]*Institute of Optics and Quantum Electronics, Max-Wien-Platz 1, 07743 Jena, Germany*

[2]*Helmholtz-Institute Jena, Fröbelstieg 3, 07743 Jena, Germany*

[3]*GSI Helmholtzzentrum für Schwerionenforschung GmbH, Planckstraße 1, 64291 Darmstadt, Germany*

(Received 13 June 2022; revised 22 February 2023; accepted 4 November 2023; published 16 January 2024)

We present experimental results which show a laser polarization-dependent contribution to electron beam pointing jitter in laser wakefield accelerators (LWFAs). We develop a theoretical model for the polarization dependence in terms of the transverse dynamics of trapped electrons, resonantly driven by bubble centroid oscillations. The latter are generated by the carrier wave phase evolution at the self-steepened laser pulse front. In the model, the polarization-dependent jitter originates from shot-to-shot fluctuations of the laser carrier envelope phase (CEP). The model is verified by particle-in-cell simulations and suggests that CEP stabilization of the driving lasers might be necessary to achieve ultimate electron pointing stability in LWFAs.

DOI: 10.1103/PhysRevResearch.6.013056

I. INTRODUCTION

Laser wakefield accelerators (LWFAs) [1] have rapidly evolved from proof of principle to a stage where they combine extremely large accelerating fields with the generation of short electron bunches of a few fs length [2–4], charge of hundreds of pC [5], and low emittance [6] with most recent work focusing on stability and reliability. A single cm-scale stage can reach energies of up to 8 GeV [7] with significantly higher energies possible in multistage systems. During the acceleration process, a highly relativistic laser pulse is focused into a plasma, thus generating a plasma wave with strong longitudinal electrical fields of 100 GV/m [8]. The transient nature of the plasma puts exacting requirements on the laser and plasma target to achieve the desired beam parameters. Controlling the phase-space properties of these transient, micron-scale accelerating structures is the focus of intense research. Major improvements have been achieved in terms of the spectrum and the emittance of the electron bunch by developing designs capable of controlling the injection process using schemes such as downramp [9], colliding pulse [10], and ionization injection [11,12]. These have achieved low energy spread, high energy, high charge, and low emittance beams with high spectral stability, essential for a high-quality accelerator. The stability of the transverse phase space, beam pointing, and source position, however, is equally critical. Experiments in strong-field QED [13–15] or LWFA-based particle colliders serve as examples, with the most exacting experiments requiring a fluctuation much smaller than beam divergence and a variation of the source position of less than the source diameter.

It is well known that the electron bunch follows the laser pulse propagation to first approximation, since the wakefield and consequently, the accelerating forces are caused by the laser pulse. Generally, pointing fluctuations have been attributed to imperfections in the reproducibility of the gas target. The pointing fluctuations of modern laser systems can be as low as 2 μrad [16]. While they are substantially smaller than electron pointing fluctuations of 500 μrad [17], they can become significant when amplifying effects due to density gradients are taken into account [18]. Sporadic density ripples or shot-to-shot density fluctuations that occurred in early gas jet designs can contribute to additional jitter. However, in the capillaries and gas cells often used nowadays, these modulations are much smaller [19] and can be neglected as a source of jitter. Other sources of pointing jitter are pulse-front tilt [20], off-axis injection of the electron bunch [21,22], and direct interaction of the laser with the electron bunch, which is used to enhance hard x-ray generation [23] or fluctuations in the position of the laser near-field. These sources of pointing fluctuation can, in principle, be avoided under typical acceleration conditions. Importantly, they are not intrinsic to the acceleration process. The question arises whether there are any further sources of pointing fluctuations occurring in the plasma accelerator itself. We note that in a homogeneous plasma, the laser generally was believed to cause a symmetric transverse electron density modulation due to the symmetric ponderomotive potential. For experiments with few-cycle pulses, which have attracted some interest for high-repetition rate generation of few MeV electrons in high-density gas targets [24–27], the situation is different. In that case, the rising intensity edge of the laser is very steep, causing an asymmetric transverse density modulation, and further, a beam pointing fluctuation due to laser carrier-envelope-phase (CEP) fluctuations [28–30].

*seidel.andreas@uni-jena.de

†b.lei@gsi.de

In this paper, we report on an instability affecting the achievable limits of beam pointing stability. We identify a mechanism intrinsic to the LWFA process coupling the laser polarization to the beam pointing for the first time and also for non-few-cycle pulses. For our conditions, the polarization-induced jitter has magnitude equal to polarization-independent contributions. The polarization dependence of the beam jitter is explained by collective betatron oscillations resonantly excited by bubble centroid oscillations (BCOs) due to an asymmetric expulsion of the background electrons in a self-steepened pulse front. This mechanism adds additional jitter in the laser polarization direction due to CEP fluctuations and will be present even in the case of an ideal laser or target. This suggests that CEP stabilization of the driving lasers might be necessary to achieve ultimate electron-pointing stability in LWFAs.

The paper is organized as follows: In Sec. II we present the experimental results on the polarization-dependent electron beam pointing from a campaign at the JETi-200 laser. In Sec. III we develop the theoretical model for the beam jitter. We discuss our results in Sec. IV and summarize in Sec. V.

II. EXPERIMENTAL RESULTS

A. Setup

The experiment was carried out at the JETi-200 laser facility at the Helmholtz Institute Jena, which delivered an energy up to $E = 2.5$ J on target at a center wavelength $\lambda_0 = 800$ nm and a pulse length $\tau = 23$ fs. Focusing with an f/24 off-axis parabolic mirror resulted in a vacuum FWHM focus diameter of 22 μm enclosing 40 % of the total energy and consequently in a normalized vector potential of $a_0 = 2.5$.

The target in this experiment was a 5.8 mm long gas cell developed at Helmholtz Institute Jena. According to fluid dynamics simulations, the gas flow from the entrance holes resulted in a 1.5 mm density upramp followed by a 5 mm constant density profile and a 1.5 mm downramp. The accelerated electrons were detected 187 cm downstream with a Kodak BioMAX scintillation screen [31], allowing a precise measurement of the transverse electron beam charge distribution and beam pointing with a resolution of 0.05 mrad by evaluating the center of a Gaussian fit to the charge distribution.

At a plasma density of $n_e = 4 \times 10^{18}$ cm^{-3} the average FWHM electron beam divergence was 1.1 mrad (see Fig. 1) with an average total charge of more than 40 pC and typical electron beam energies up to 600 MeV (see Fig. 2). For these conditions, theoretical scalings predict an accelerating field of 150 GV/m [8,32] implying an acceleration length of 4 mm and consequently injection at the front of the gas cell for both injection mechanisms.

B. Electron beam pointing jitter

In the following we present the experimental data showing the polarization-dependent beam pointing jitter. Figure 3 shows the experimental data for the electron pointing angles of 50 consecutive shots as symbols in [(a)–(f)], excluding shots without electrons. Each data set was taken on a single run with the laser being linearly polarized either horizontally or vertically. The laser polarization was controlled by a $\lambda/2$ wave plate in front of the final focus parabola. Data were taken for LWFAs with pure He [(a)–(c)] and a 95 %He–5 %N_2 gas mixture [(d)–(f)], respectively. In addition to the individual shots, the total rms jitter for horizontal and vertical laser polarization is shown as an ellipse in Figs. 3(a)–3(f). When comparing the shapes of the ellipses for horizontal and vertical laser polarization within the same dataset, the ellipses tend to grow in the direction of polarization for most cases (see also Fig. 4). This is the behavior expected for a pointing jitter contribution along the laser polarization direction superimposed on an underlying polarization-independent jitter.

Figure 4 provides a schematic of the interplay of the two jitter components for the case of symmetric and horizontally dominated polarization-independent contributions.

In our data (Fig. 3) the overall horizontal pointing jitter tends to be larger than the vertical jitter. This effect arises mainly due to the laser pointing fluctuating of JETi-200 being

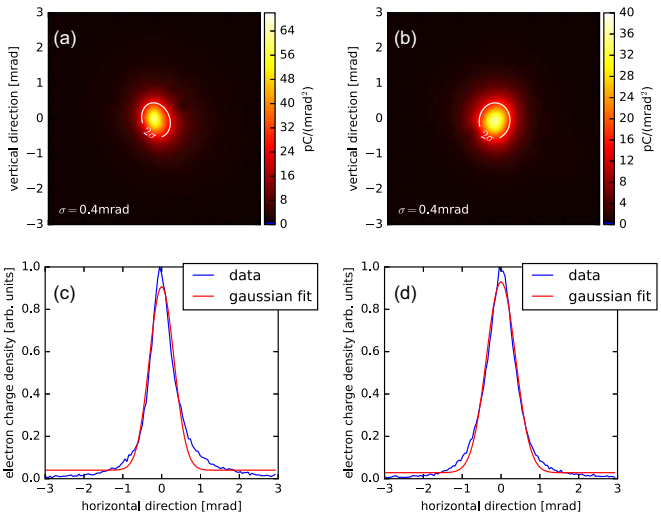

FIG. 1. Representative electron beam profile with σ indicating the rms electron spot radius. (a) Profile for data set in Fig. 3(e) (ionization injection, $n_e = 4.3 \times 10^{18}$/cm^3) and (b) profile for data set in Fig. 3(b) (self-injection, $n_e = 4.5 \times 10^{18}$/cm^3). (c) and (d) indicate a lineout (vertical direction = 0 mrad) with Gaussian fit through the center of the beam profile for the respective spots in (a) and (b).

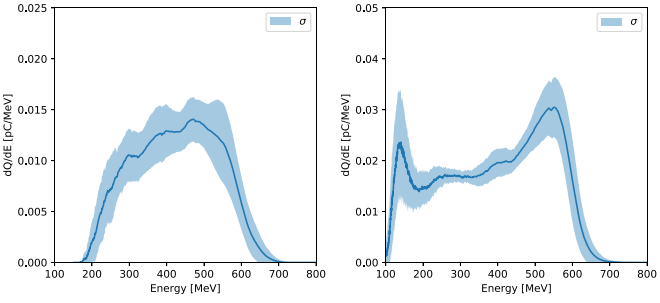

FIG. 2. Left panel: Mean electron beam spectrum for a set of 30 consecutive shots for self-injection ($n_e = 4.5 \times 10^{18}$/cm^3). Right panel: Mean electron beam spectrum for a set of 30 consecutive shots for ionization injection ($n_e = 3.8 \times 10^{18}$/cm^3). σ indicates the rms value of dQ/dE at the respective energy.

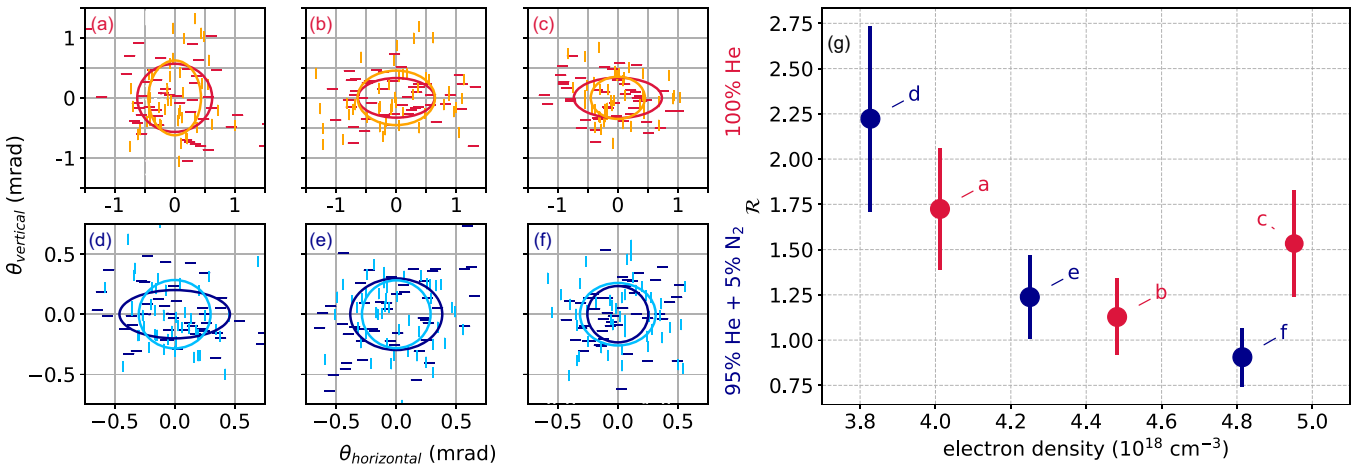

FIG. 3. [(a)–(f)] Experimentally measured electron pointing data for vertical (vertical bars) and horizontal (horizontal bars) laser polarization. Each symbol corresponds to one shot for pure helium, i.e., self-injection [(a)–(c)], and 95% helium 5% nitrogen mixture (ionization injection) [(d)–(f)], at various plasma densities. The ellipses indicate the rms jitter of the electrons in respective polarization directions. Note that the axes are scaled differently in [(a)–(c)] compared to [(d)–(f)]. (g) Magnitude of laser polarization induced electron pointing jitter, with $\mathcal{R}$ defined in Eq. (1) and $\mathcal{R} > 1$ implying a positive correlation between polarization direction of the laser and an increased pointing jitter.

stronger by a factor of 6 in the horizontal plane at the laser output. While these laser pointing fluctuations are much smaller than the electron beam pointing and on the order of tens of μrad, they are known to be magnified by transverse refractive index gradients in plasma density gradients at the entry and exit of the gas cell, which act as defocusing lenses [18,33]. Since the laser pointing jitter is *polarization independent* this affects both horizontal and vertical laser polarization cases alike, and one expects the electron pointing jitter to be larger in the horizontal direction, as illustrated in Fig. 4.

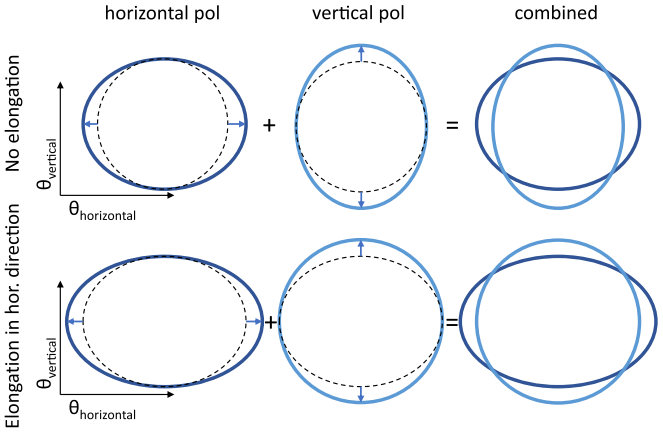

FIG. 4. Schematic showing the expected change in shape of the jitter ellipses evolving from polarization-dependent and polarization-independent contributions. Top row: In an idealized case with *symmetric* polarization-independent jitter component (dashed circles) the added polarization contribution (arrows) leads to the total polarization ellipse's major axis being aligned with the laser polarization direction. Bottom row: If the polarization-independent jitter component is *systematically larger in the horizontal direction* (dashed ellipses) the ellipses with the added polarization contribution may appear round or with the major axis along the horizontal direction even for vertical laser polarization. The polarization-dependent jitter component is clearly visible from the change in ellipse shape and by comparing the ratio of the ellipses with different laser polarization.

To obtain a quantitative analysis of the data, it is assumed that the total electron pointing jitter, $\sigma_{TX} = \sqrt{\sigma_{0X}^2 + \sigma_P^2}$, consists of a polarization-independent part σ_{0X} and a polarization-dependent part σ_P, with X indicating either the horizontal (H) or vertical (V) direction. We assume the polarization-dependent contribution σ_P to be independent of the laser polarization orientation. Following from the discussion above, at JETi-200 we have $\sigma_{0H} > \sigma_{0V}$.

The quantities σ_{0X} and σ_{TX} are accessible directly from the experimental data in Fig. 3 with two orthogonal laser polarization orientations. For example, for horizontal polarization the horizontal and vertical sizes of the covariance ellipse of the pointing data yield σ_{TH} and σ_{0V}, respectively. To avoid any time sensitive drift, the data shots were collected consecutively for each plasma density in both horizontal and vertical laser polarization. The electron pointing data were analyzed for each set using bootstrapping to determine the mean jitter and its uncertainty [34]. As a measure for the relative polarization-induced pointing jitter, we define the double ratio

$$\mathcal{R} = \frac{\sigma_{TH}}{\sigma_{0H}} \frac{\sigma_{TV}}{\sigma_{0V}} = \frac{\sqrt{\sigma_{0H}^2 + \sigma_P^2}}{\sigma_{0H}} \frac{\sqrt{\sigma_{0V}^2 + \sigma_P^2}}{\sigma_{0V}}, \qquad (1)$$

which is presented in Fig. 3(g). A ratio of $\mathcal{R} = 1$ corresponds to an absence of any polarization dependence, while $\mathcal{R} > 1$ implies a larger beam jitter in the laser polarization axis, which is observed for most data sets.

Our data also show a density dependence of σ_P, which can be more clearly seen from additional Bayesian analysis (for more details on the method see Appendix A) in Fig. 5. Utilizing the latter method allowed us to directly infer the polarization-dependent jitter contribution σ_P, e.g., $\sigma_P =$ 0.42 mrad (0.25 mrad) for dataset (d) and decreasing with increasing density (Fig. 5). From the Bayesian analysis, we find the mean polarization-independent jitter as $\sigma_0 = 0.44$ mrad

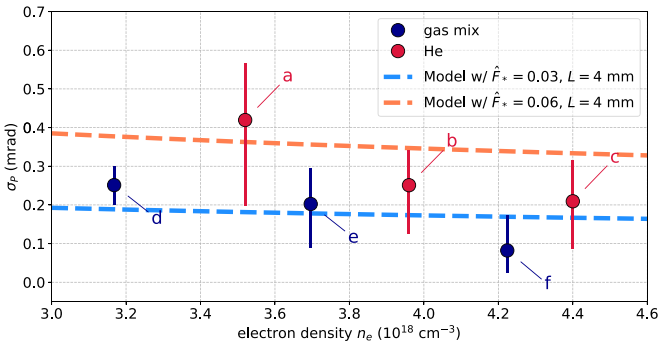

FIG. 5. Magnitude of the polarization-dependent electron pointing jitter contribution σ_P for the data presented in Fig. 3 and comparison with the BCO model derived below.

(0.26 mrad) for pure He (gas mix), quite independent of the density in the investigated range. It is worth noting that the polarization-dependent jitter contribution has magnitude equal to the polarization-independent contribution.

III. THEORETICAL MODEL FOR THE POLARIZATION-DEPENDENT POINTING JITTER

Possible mechanisms that couple the laser polarization to the electron trajectories are (i) a polarization-dependent injection mechanism [28,35–38], (ii) electron interactions with the laser within the wake, or (iii) coupling between the laser polarization and the bubble trajectory due to propagation effects in the plasma resulting in the bubble oscillating as a whole. The first hypothesis is unlikely as both injection mechanisms follow a general density-dependent trend [Figs. 3(g) and 5], although the absolute jitter σ_T for self and ionization injection differ slightly. The second hypothesis is unlikely since no signs of direct laser-electron interaction in the electron spectra or the charge distribution were detected. Indeed, the strongest polarization dependence is observed at low densities, which corresponds to the longest dephasing length [8] and the longest distance from the electrons to the laser throughout propagation. This trend is the opposite of what would be expected for this hypothesis, where the onset of the effect could only take place at a threshold density, after which dephasing allows the electrons to interact directly with the laser. We also note that particle-in-cell (PIC) simulations show polarization-dependent oscillations even for idealized external injection where the laser field plays no role, as shown in Fig. 10.

The question therefore arises regarding the mechanism that explains the observed polarization dependence of the beam-pointing jitter. We will answer this now by developing a theoretical model in which the pointing jitter emerges due to bubble centroid oscillations resonantly exciting collective electron betatron oscillations.

In the following, frequencies are normalized to the plasma frequency $\omega \to \omega/\omega_p$, distances are normalized to the plasma skin depth $x \to k_p x$, times to the plasma frequency $t \to \omega_p t$, and we introduce $\gamma_p^2 = n_{\rm crit}/n_e$ and $\zeta = z - ct$.

A. Excitation of bubble centroid oscillations

We recall that on a subcycle level the laser-driven electron motion is strongly dependent on the polarization. When only a few cycles are active in ejecting the plasma electrons, the side receiving more electrons changes periodically due to the difference between the laser phase and the group velocity. The excited plasma bubble will react to this by undergoing bubble centroid oscillations (BCOs) in the laser polarization plane; consequently, the bubble wobbles. This phenomenon was first derived in Ref. [39] for the case of few-cycle pulses. From this analysis, it is clear that BCOs can only be efficiently excited if the driving pulse possesses pronounced single-cycle features. In the case of LWFA accelerators, the laser pulses usually do not meet this criterion initially. However, self-steepening of the laser pulse front to a few-cycle rise time due to nonlinear plasma response typically accompanies bubble formation. Significant front steepness can be expected when the front half of the pulse has been depleted, approximately after $L \sim \gamma_p^2 c\tau/2 \sim 1.5$–$2$ mm [40,41]. The period of the BCO is determined by the laser carrier wave phase changing by 2π at the pulse front [28,39]. The scaling of the BCO frequency can be estimated by $\omega_{\rm bc} = \omega_L(v_{ph} - v_{gr})$, and using the linear plasma response results for the laser phase (v_{ph}) and group (v_{gr}) velocity. This yields $\omega_{\rm bc} = \omega_L/\gamma_p^2$, where $\gamma_p = \sqrt{n_{\rm crit}/n_0}$. However, the plasma refractive index and hence laser dispersion in a plasma becomes nonlinear for $a_0 \gtrsim 1$ due to relativistic self-guiding and self-channeling [8,32]. These effects do not affect the density scaling $\propto 1/\gamma_p^2$, but they affect the numerical factor of proportionality. In addition, due to pulse-front etching the relevant location of the steep pulse front moves backward through the pulse with the etching velocity $v_{\rm etch} \propto 1/\gamma_p^2$ [40]. This effect also does not change the scaling but again modifies the factor of proportionality, thus $\omega_{\rm bc} = c_{\rm bc}\omega_L/\gamma_p^2$, with $c_{\rm bc} = \mathcal{O}(1)$. Eventually, the factor $c_{\rm bc}$ was determined by particle-in-cell simulations for plasma densities, laser spot sizes, and laser intensities close to the experimental conditions. It was found to be approximately $c_{\rm bc} = 1.5$, which was then used in the subsequent modeling of the beam pointing jitter. In order to find the amplitude of the bubble centroid oscillations, $x_{\rm bc}(t) = a_{\rm bc}\sin(\omega_{\rm bc}t + \phi_{\rm bc})$, we need to solve the equation of motion for the plasma electrons [39]:

$$\frac{d(\vec{p} - \vec{a})}{dt} = \vec{\nabla}\Phi - \vec{\nabla}(\vec{v}\cdot\vec{a}).$$

We use the Coulomb gauge where the scalar potential $\Phi = 0$ and the laser vector potential is linearly polarized $a_x = a_0\cos(\zeta + \phi_{\rm CE})h(\zeta)e^{-(x^2+y^2)/w_0^2}$, with $\zeta = \gamma_p(z - ct)$, temporal pulse envelope $h(\zeta)$ and transverse size w_0. Moreover, the wide pulse approximation $\gamma_p w_0 \gg a_0 \gg 1$ is assumed to hold [39]. The formal derivation of the bubble centroid oscillation was laid out in Ref. [39]. The central idea is to describe the plasma electron response to the laser pulse in a series $x = x^{(0)} + \epsilon x^{(1)} + \epsilon^2 x^{(2)}$, $p_x = p_x^{(0)} + \epsilon p_x^{(1)} + \epsilon^2 p_x^{(2)}$, where the formal expansion parameter $\epsilon = a_0/\gamma_p w_0$ is the electron oscillation amplitude over the laser spot size. We define the normalized transverse coordinate as $X = \gamma_p(x - x_0)/a_0$, with x_0 as the initial electron position and $p_x^{(j)} = -a_0 dX^{(j)}/d\zeta$. By expanding the vector potential to the second

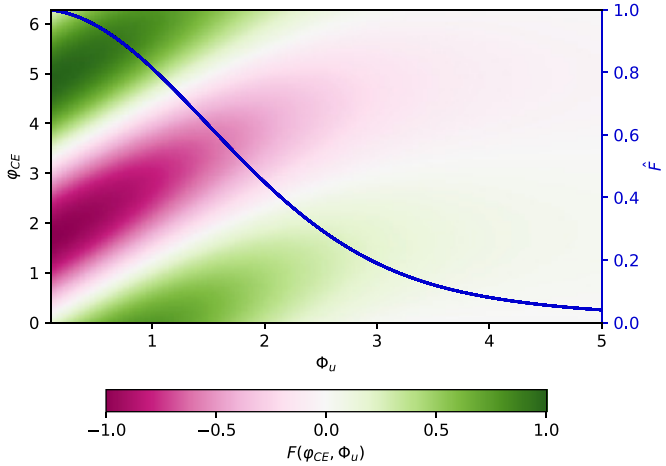

FIG. 6. Contour plot of the functions F and $\hat{F} = \max_{\phi_{\rm CE}} F$ determining the amplitude of bubble centroid oscillations.

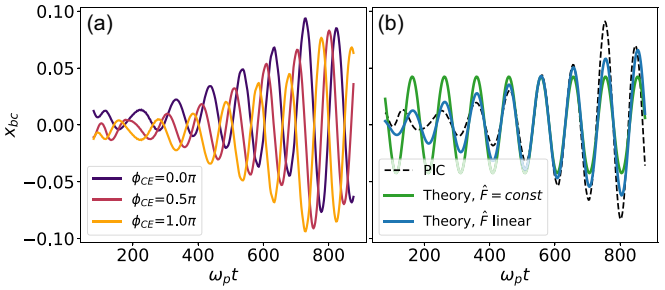

FIG. 7. PIC simulation results showing (a) the dependence of the BCO on the CEP and (b) a comparison with the theoretical scaling where $\omega_{\rm bc} = 1.5/\gamma_p$, and $\hat{F} = 0.25 = $ const. for the green curve. The blue curve has a linearly increasing $\hat{F}$, modeling a dynamically evolving pulse front, which agrees much better with the PIC simulations.

order, $a_x = a_0 f(\zeta)(1 - \mu X + \nu X^2)$, the electron equation of motion can be written as

$$\frac{d^2X}{d\zeta^2} + \frac{df}{d\zeta}(1 - \mu X + \nu X^2) - \frac{2\nu g}{a_0^2} p_z = 0. \tag{2}$$

Here, $\mu = 2x_0 a_0/(\gamma_p w_0^2) \sim \epsilon$, $\nu = a_0^2(2x_0^2/w_0^4 - 1/w_0^2)/\gamma_p^2 \sim \epsilon^2$, and $f(\zeta) = h(\zeta)e^{-\bar{x}_0^2/w_0^2}$. By solving (2) perturbatively it is easy to show that the zeroth order term is the response of the electrons to the plane wave laser oscillations, $p^{(0)} = a_0 f(\zeta)$ and $X^{(0)} = -g(\zeta)$, with $g(\zeta) = \int_0^\zeta f(\zeta')d\zeta'$. The first order $p^{(1)}$ is the ponderomotive deflection, and $p^{(2)}$ is a correction to it, which is in fact polarization dependent [39]. The latter term is causing the BCO, eventually. What is most relevant for the derivation of the BCO are the values of $p^{(j)}$ after the laser pulse has passed, for which one can easily show that $p^{(0)} = 0$. The other terms read $p^{(1)} \simeq \mu \int f^2 d\zeta$ and $p^{(2)} \simeq -(3\nu + \mu^2) \int f^2 g d\zeta$. Those have different symmetry with regard to the initial transverse position x_0 of the electron away from the laser beam axis. The ponderomotive term $p^{(1)}$ always pushes electrons away from the beam axis (the location of highest intensity) irrespective of x_0, i.e., $p^{(1)}(-x_0) = -p^{(1)}(x_0)$. Contrarily, it was found that $p^{(2)}$ has the symmetry $p^{(2)}(-x_0) = +p^{(2)}(x_0)$, i.e., the correction $p^{(2)}$ deflects electrons into the same direction on both sides of the beam center, and alternating each laser half cycle. The amplitude of the BCO is estimated by the magnitude of the polarization-dependent subcycle deflection $p^{(2)}$ in comparison to the ponderomotive expulsion $p^{(1)}$, i.e., by a slight change of the typical electron deflection angle by $\Theta \sim p^{(2)}/p^{(1)} \sim a_0 \hat{F}/\gamma_p w_0$. Here we introduced the pulse-front steepness parameter $\hat{F} = \max_{\phi_{\rm CE}} F$ with $F = \int f^2 g\, d\zeta / \int f^2\, d\zeta$. The functions F and $\hat{F}$ are nonvanishing only if the temporal pulse envelope profile changes rapidly on the wavelength scale. We present plots for F and $\hat{F}$ in Fig. 6, where we model the pulse envelope as $h(\zeta) = e^{-\zeta^2/2\Phi_u}\theta(\zeta) + e^{-\zeta^2/2\Phi_d}\theta(-\zeta)$, with the step function $\theta(\cdot)$. We use a short pulse-front duration Φ_u and a long pulse back duration $\Phi_d = 25$. Note that the result is nearly independent of Φ_d for $\Phi_d > 5$. The contour plot of the functions F clearly exhibits the CEP dependence. The line plot of $\hat{F} = \max_{\phi_{\rm CE}} F$ shows that $\hat{F}$ rapidly approaches zero for longer pulse fronts. Thus, according to expectation, the parameter $\hat{F}$ is nonvanishing only if the temporal pulse profile changes rapidly on the wavelength scale. This is relevant, e.g., for few-cycle pulses [28,39], or pulses which have undergone severe pulse-front steepening and thus acquired single-cycle features [40–43].

Finally, the BCO amplitude $a_{\rm bc}$ can be estimated as $a_{\rm bc} \sim \Theta R$, where R is the bubble radius for which we use the scaling $R = 2\sqrt{a_0}$ [32]. This yields $a_{\rm bc} \sim 2a_0^{3/2}\hat{F}/\gamma_p w_0$. If we further assume a matched focal spot $w_0 = R$ we find the scaling for the BCO amplitude $a_{\rm bc} \sim a_0 \hat{F}/\gamma_p$.

In summary, the bubble centroid oscillates according to $x_{\rm bc}(t) = a_{\rm bc}\sin(\omega_{\rm bc}t + \phi_{\rm bc})$, where the scalings of amplitude $a_{\rm bc} \sim a_0\hat{F}/\gamma_p$ and frequency $\omega_{\rm bc} \sim 1/\gamma_p$ follow from theory, but the phase $\phi_{\rm bc} = \phi_{\rm CE} + \phi_0$ is *a priori* unknown since it contains contributions from the laser carrier-envelope phase $\phi_{\rm CE}$ plus an offset ϕ_0. To verify if the theoretically predicted oscillations are present in PIC simulations, the bubble centroid was defined in the latter via zero crossing of the transverse focusing force $E_x - B_y$. The BCO according to the model is in good agreement with the simulations; see Fig. 7. Details on the numerical setup can be found in Appendix B.

B. Betatron-BCO-resonance induced beam pointing jitter

We now explain how BCOs cause polarization-dependent beam jitter via a (resonant) excitation of collective betatron oscillations of trapped electrons in the laser polarization plane. If the bubble oscillates transversely, it is clear that the transverse confining potential behaves as $\sim[x - x_{\rm bc}(t)]^2$. The trapped electron dynamics is thus governed by the driven oscillator equation [44],

$$\ddot{x} + \frac{\dot{\gamma}}{\gamma}\dot{x} + \omega_\beta^2 x = \omega_\beta^2 x_{\rm bc}(t), \tag{3}$$

where the betatron frequency $\omega_\beta(t) = 1/\sqrt{2\gamma(t)}$. As the electrons are accelerated, ω_β slowly decreases as the Lorentz factor γ increases. Since initially $\omega_\beta > \omega_{\rm bc}$, this means ω_β eventually drops below $\omega_{\rm bc}$ as the maximum energy gain of electrons in a LWFA is $\gamma_{\rm max} \sim \frac{2}{3}a_0\gamma_p^2$ [32]. Therefore, at some

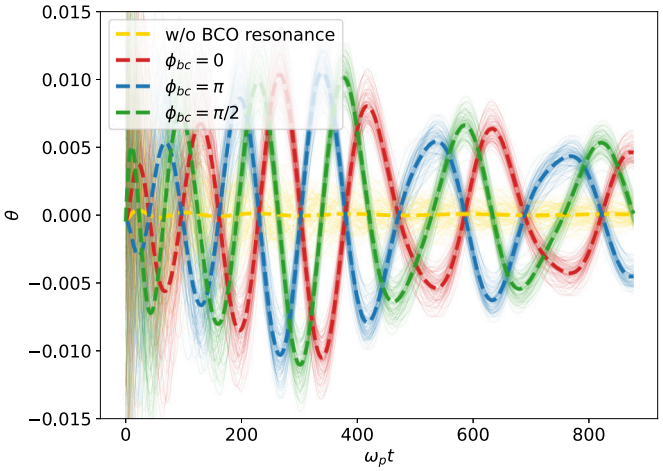

FIG. 8. Excitation of collective betatron oscillations leads to a strong variation of the beam angle θ along the polarization direction. Thin curves are individual electrons; thick dashed curves are ensemble averages. Without the BCO resonance, $x_{\rm bc} = 0$ (yellow curves), the beam centroid angle is almost zero. With the BCOs active (red, blue, green), the beam is collectively excited, where the phase of that oscillation and final value of θ depend on $\phi_{\rm bc}$.

time during the acceleration process, the betatron oscillations will become resonant with the BCO, $\omega_\beta(t) \sim \omega_{\rm bc}$, at which the external driving force strongly increases the beam pointing angle $\theta = \dot{x}$ in the laser polarization plane.

To demonstrate this, we have solved numerically Eq. (3) for a bunch of electrons with randomly distributed initial values x_0, θ_0, all injected at the same time $t_i = 0$. The results are shown in Fig. 8. Without the BCO resonance active (yellow curves), i.e., setting $x_{\rm bc} = 0$, individual electrons perform betatron oscillations (thin yellow curves), but the beam centroid angle is almost zero (dashed yellow curve). With the BCOs active, i.e. in the case when a self-steepened laser pulse has excited bubble centroid oscillations, $x_{\rm bc} \neq 0$, the electron beam betatron motion is collectively excited. In addition to the individual electron betatron oscillations now also the beam centroid trajectory oscillates (red, blue, and green dashed curves). The phase of that oscillation depends on the value of $\phi_{\rm bc}$. An uncontrollable shot-to-shot fluctuation of $\phi_{\rm CE}$, hence $\phi_{\rm bc}$, leads to shot-to-shot fluctuations of θ at the end of the accelerator, thus the beam pointing jitter.

We now estimate the size of the beam pointing jitter analytically within our model. The Wentzel-Kramers-Brillouin (WKB) solution [45] of Eq. (3) is given by

$$x(t) = \sqrt{\frac{\omega_\beta(t)}{\omega_\beta(t_i)}}\left(x_0 \cos\varphi(t) + \frac{\theta_0}{\omega_\beta(t_i)} \sin\varphi(t)\right) + \sqrt{\omega_\beta(t)} \int_{t_i}^{t} \sqrt{\omega_\beta(t')} \sin[\varphi(t) - \varphi(t')] x_{\rm bc}(\phi_{\rm bc}, t')\, dt' \tag{4}$$

with betatron phase advance $\varphi(t) = \int_{t_i}^{t} \omega_\beta(t')\, dt'$ and t_i is the injection time.

To simplify the argument, we assume the injection time interval is short compared to the BCO period. (The general case is discussed in Appendix C.) It is then sufficient to consider

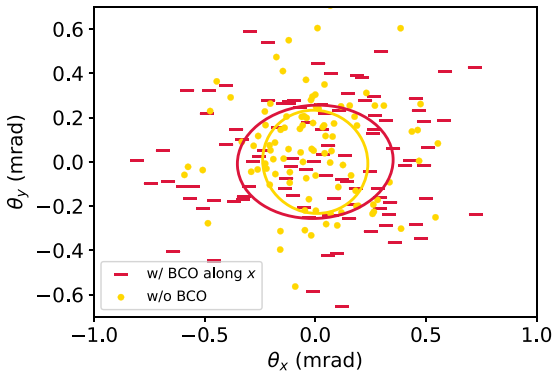

FIG. 9. Polarization-dependent pointing jitter calculated using the betatron-BCO-resonance model. Without BCO (yellow symbols) the jitter is the same along the x and y axes, while BCOs ($\omega_{\rm bc} = 1.5/\gamma_p$, $\hat{F} = 0.03$, red symbols) increase the pointing jitter along x.

the trajectory of the beam centroid only as a representative of the whole beam. For a beam with initial centroid $\bar{x}_0 = \bar{\theta}_0 = 0$ the homogeneous part of the WKB solution in the first line of Eq. (4) vanishes. The pointing angle is determined solely by the inhomogeneous contribution, i.e., the collective betatron oscillations excited by the BCO,

$$\theta(t) = \omega_\beta^{3/2}(t) \int_{t_i}^{t} \sqrt{\omega_\beta(t')} \cos[\varphi(t) - \varphi(t')] x_{\rm bc}(\phi_{\rm bc}, t')\, dt'. \tag{5}$$

To calculate the pointing jitter, we have to evaluate averages over the unknown fluctuating phase $\phi_{\rm bc}$ in $x_{\rm bc}$ (denoted by $\langle \cdots \rangle$). The pointing jitter is determined by the second moment $\sigma_P^2 := \Delta\theta^2 = \langle (\theta - \langle\theta\rangle)^2 \rangle$. It is straightforward to show that the inhomogeneous contribution of the WKB solution in Eq. (4) vanishes under this average. Thus, $\theta - \langle\theta\rangle$ is given by Eq. (5) for arbitrary initial conditions $\bar{x}_0$, $\bar{\theta}_0$. We find for the second moment

$$\sigma_P^2 = \frac{\omega_\beta^3(t)}{8} \left| \int_{t_i}^{t} dt' \sqrt{\omega_\beta(t')}\, a_{\rm bc}(t') e^{-i(\varphi_{t'} - \omega_{\rm bc} t')} \right|^2. \tag{6}$$

This equation predicts the size of the beam-pointing jitter as a function of the amplitude and frequency of the bubble centroid oscillation. For longer acceleration times, it predicts a decrease of the jitter as $\gamma^{-3/2}$ due to the decrease of the betatron frequency via the prefactor $\omega_\beta^3(t)$. Using a saddle point approximation of Eq. (6), we find the scaling $\sigma_P^2 \sim L^{-3/2} \hat{F}_\star^2 \gamma_p^{3/2}$, where L is the acceleration length and $\hat{F}_\star$ is the pulse-front steepness parameter at resonance. The predicted density dependence $\sigma_P^2 \sim n_e^{-3/4}$ is in reasonable qualitative agreement with the experimental findings (see Fig. 5).

Results for the beam pointing jitter obtained from the betatron-BCO-resonance model are shown in Fig. 9. Parameters were chosen to match dataset (d) of Fig. 3: $\gamma_p = 23$, $L = 4$ mm, $a_0 = 4$. The initial conditions (x_0, θ_0) for the electrons were chosen to yield a polarization-independent jitter of $\sigma_0 = 0.26$ mrad if the BCO is turned off. With the BCO active, the jitter in the polarization direction increases to $\sigma_T = 0.35$ mrad, hence $\sigma_P = 0.23$ mrad. This shows that the experimentally observed polarization-dependent jitter can be

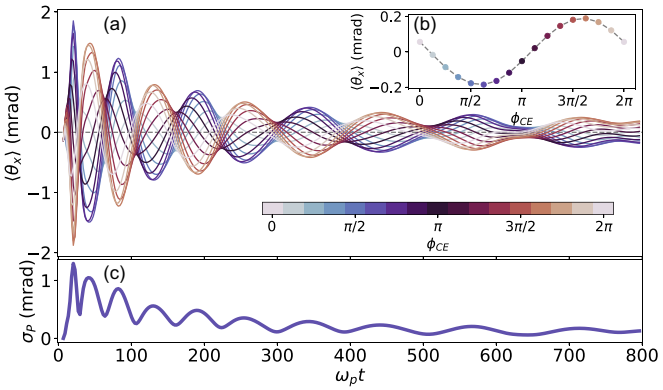

FIG. 10. PIC simulation results for the CEP dependence of the beam pointing during propagation in plasma for an externally injected beam (a), pointing at the end of the simulation at $\omega_p t = 800$ (b), and evolution of rms beam jitter (c).

understood qualitatively and even quantitatively in terms of the betatron-BCO resonance model.

IV. DISCUSSION

The CEP dependence of electron beam pointing is confirmed using a large set of PIC simulations, as shown in Fig. 10. In these simulations, we externally injected an electron beam centrally into a wakefield to eliminate potential CEP effects from the injection. The laser pulse was defined here with a "triangular" envelope to mimic the shape of the pulse front after self-steepening. It is clear that polarization and CEP effects could also modify the injection process, as was discussed in [28]. The external injection simulations were done to demonstrate explicitly that the BCOs *alone* can explain the experimental findings. We also performed simulations with ionization injection, which show a qualitatively similar CEP dependence as the external injection case (see also Appendix B).

Our model also allows different experimental cases [(a)–(f)] to be explained. We note that the model reproduces the general trend to smaller absolute pointing jitter for higher densities (corresponding to a longer propagation in units of $\omega_p t$ in Fig. 10).

In general, the BCOs contribute to both beam pointing jitter and emittance [28,39]. The emittance contribution vanishes for short injection lengths, but the pointing does not. That means that, by our assumption of a short injection length above, we have explicitly singled out the jitter contribution. (The effect of a long injection length is discussed in more detail in Appendix C.) Modern gas targets are often designed for localized injection [46]. However, this is insufficient to achieve stable pointing, as shown in Fig. 10. For constant initial CEP all phases are constant, and the injection direction is also reproducible shot to shot. Controlling the CEP phase to within 500 mrad [47] as shown in Fig. 10(b) constrains the polarization induced jitter to below 50 μrad. We note that longer drive pulses do not, in general, eliminate the CEP-dependent effect, as a steep pulse front occurs even for initially long pulses, due to the nonlinear pulse evolution in the plasma.

Additional polarization and CEP-dependent contributions to the pointing jitter can come from the injection process if the driving laser pulse contains single-cycle features already during injection, e.g., for LWFAs with single-cycle pulses [28,30]. The model put forward in this paper, however, suggests that CEP fluctuation can play an essential role for LWFA pointing stability also beyond single-cycle pulses.

V. SUMMARY

In conclusion, we have experimentally and theoretically identified a mechanism intrinsic to the LWFA process that couples both CEP and polarization to the electron beam pointing. This mechanism is fundamental to laser wakefield accelerators in the sense that the regime of pulse-front etching and steepening is necessary for the efficient operation of LWFAs and eliminating the instability requires additional CEP stabilization. A stable operation can nonetheless be achieved if the phase of the oscillation at the output of the accelerator is kept constant, requiring not only a sufficiently reproducible target density profile and injection region but also a CEP-stable drive laser.

ACKNOWLEDGMENTS

The authors gratefully acknowledge the Gauss Center for Supercomputing e.V. [48] for funding this project by providing computing time through the John von Neumann Institute for Computing (NIC) on the GCS Supercomputer JUWELS at Jülich Supercomputing Center (JSC). Particle-in-cell simulations were performed with SMILEI [49]. The authors thank G. Schäfer for operating the JETi-200 laser system. The research leading to the presented results received additional funding from the European Regional Development Fund and the State of Thuringia (Contract No. 2019 FGI 0013).

APPENDIX A: BAYESIAN INFERENCE

In addition to the ratio-of-ellipses measure $\mathcal{R}$ discussed in the main text, Bayesian inference was used to estimate the value of the polarization-dependent jitter contribution [50]. The generative model for the data is Gaussian with tilted covariance ellipses, in which the polarization-dependent jitter contribution σ_P is attributed to either H or V depending on the laser polarization direction being horizontal or vertical. The unpolarized jitter contribution is assumed to have the same magnitude along the major and minor axes for both H and V cases, but we allow for a relative tilt of those axes for H and V independently. The data are the tuples $D = (x_H, y_H, x_V, y_V)$, where over each dataset the average position is normalized to zero, i.e., they represent the residuals $x_H = X_H - \mu_H$, etc.

The log-likelihood of this model is given by

$$\ln \mathcal{L}(D|\Theta) = -\frac{1}{2}\sum_{\text{data}} \left[(x_H, y_H)C_H^{-1}(x_H, y_H)^T + (x_V, y_V)C_V^{-1}(x_V, y_V)^T + \ln\det(C_H) + \ln\det(C_V)\right] \tag{A1}$$

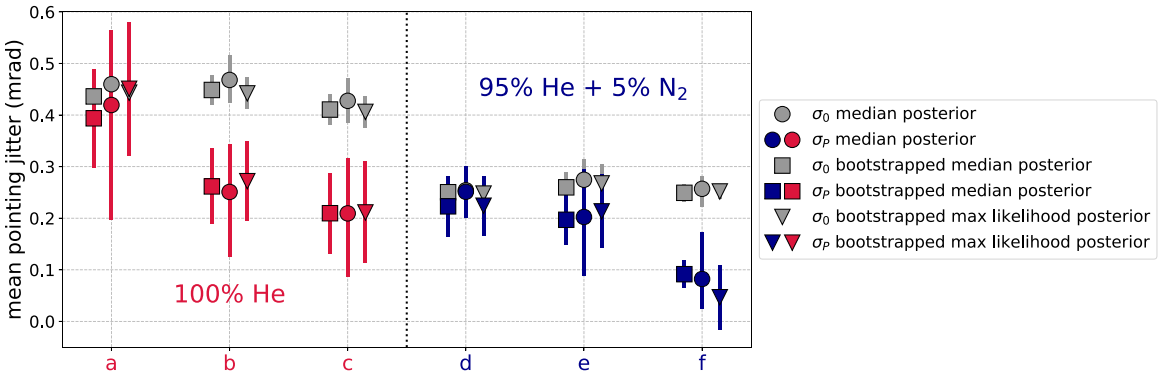

FIG. 11. Markov-chain Monte Carlo Bayesian inference [50] of the polarization-dependent contribution to the pointing jitter σ_P for the datasets (a)–(f) (cf. Fig. 3) as red or blue symbols; grey symbols are the polarization *independent* jitter contribution $\sigma_0 = \sqrt{\sigma_a \sigma_b}$ as the geometric mean of the major and minor axes. Circles are the median of the posterior distribution (error bars range from 15th to 85th percentiles). Square and triangle symbols are for a bootstrapping analysis where squares are the bootstrapped median and triangles the bootstrapped maximum posterior. Error bars represent the standard deviation of the mean of the latter two cases.

with the horizontal and vertical covariance matrices

$$C_H = \frac{1}{2}\begin{pmatrix} \sigma_a^2 + \sigma_b^2 + (\sigma_a^2 - \sigma_b^2)\cos 2\varphi_H + 2\sigma_P^2 & (\sigma_a^2 - \sigma_b^2)\sin 2\varphi_H \\ (\sigma_a^2 - \sigma_b^2)\sin 2\varphi_H & \sigma_a^2 + \sigma_b^2 - (\sigma_a^2 - \sigma_b^2)\cos 2\varphi_H \end{pmatrix}, \tag{A2}$$

$$C_V = \frac{1}{2}\begin{pmatrix} \sigma_a^2 + \sigma_b^2 + (\sigma_a^2 - \sigma_b^2)\cos 2\varphi_V & (\sigma_a^2 - \sigma_b^2)\sin 2\varphi_V \\ (\sigma_a^2 - \sigma_b^2)\sin 2\varphi_V & \sigma_a^2 + \sigma_b^2 - (\sigma_a^2 - \sigma_b^2)\cos 2\varphi_V + 2\sigma_P^2 \end{pmatrix}. \tag{A3}$$

Results from the Bayesian inference, in which we used Markov-chain Monte Carlo to infer the model parameters [50], are summarized in Fig. 11. The polarization independent jitter contribution, defined as the geometric mean $\sigma_0 = \sqrt{\sigma_a \sigma_b}$, has a constant value of approximately 0.44 mrad for 100% He gas, while for the gas mixture with ionization injection it is smaller at approximately 0.26 mrad. We found the polarization-dependent contribution to the beam jitter σ_P in some datasets [(a), (d), and (e)] being almost as large as the unpolarized jitter contribution. With increasing plasma density, the polarization-dependent jitter contribution decreases while the polarization-independent jitter remains constant. For dataset (f) the Bayesian analysis shows no significant polarization-dependent jitter, which is consistent with the analysis in Fig. 3; see Fig. 12.

APPENDIX B: NUMERICAL DETAILS ON THE PARTICLE-IN-CELL SIMULATIONS

The PIC simulations for this study were performed using SMILEI [49]. The simulations for Fig. 7 were performed with the following parameters: The simulation box was $64\lambda \times 128\lambda$ with a resolution of $\lambda/32$ ($\lambda/12$) in the longitudinal (transverse) direction. Laser parameters were $a_0 = 4$, $w_0 = 12$ μm, a short rising edge of 0.5 μm HWHM (half width at half maximum), and a long falling edge with 4 μm FWHM. The plasma density was $n = 2.3 \times 10^{18}$ cm^{-3}, corresponding to $\gamma_p = 23.56$. The numerical curves for the bubble centroid oscillation were found by determining the zero crossing of $E_x - B_y$ at a fixed lineout location ζ_0 approximately at the center of the first wakefield bucket.

For Fig. 10 the simulation box had a size of $64\lambda \times 128\lambda$, with a spatial step size of $\lambda/32$ in all directions. The laser pulse was launched from the left wall with $a_0 = 4$, $w_0 = 14$ μm, $\lambda = 800$ nm, with a vacuum focus position at the end of a 50 μm linear entry ramp. The initial pulse shape was initialized with a short rising edge corresponding to 1 μm HWHM and a long falling edge with 4 μm HWHM. After the entry ramp, the background plasma had a constant density of $n_e = 2.3 \times 10^{18}$ cm^{-3}, corresponding to $\gamma_p = 27.48$, with 16 particles per cell. The witness electron beam is externally injected from the left wall centrally on the beam axis with 64 particles per cell using a particle injector. The beam had the

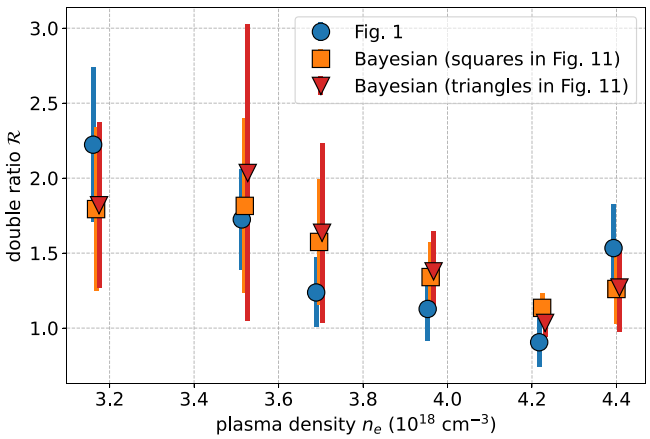

FIG. 12. Comparison of the double ratio $\mathcal{R}$, Eq. (1), evaluated as in Fig. 3 (blue circles), and deduced via Bayesian inference (squares and triangles).

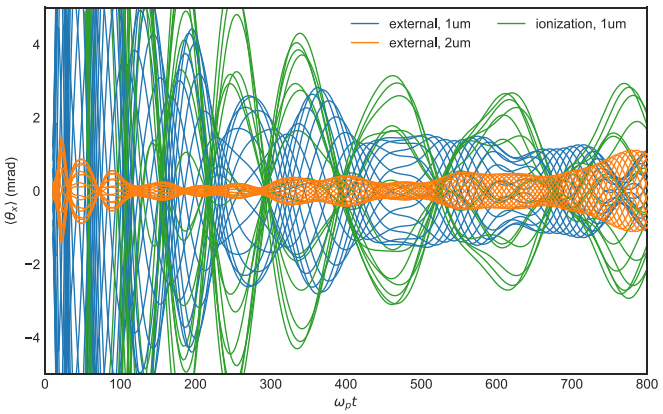

FIG. 13. Simulations showing the beam pointing for ionization injection (1 micron pulse front length) and external injection (pulse front length 1 and 2 microns). The different curves in each color are for different CEP values.

following initial properties: Transverse rms beam size 1 μm, normalized temperature 0.08, initial Lorentz factor $\gamma_0 = \gamma_p/2$.

In Fig. 13 we compare PIC simulation results for the beam pointing fluctuations for ionization injection and for external injection with different initial pulse-front lengths. The different curves in each color are for a variation of the laser carrier-envelope phase. Even though the angular variation $\langle\theta\rangle$ can be very different in the early stages of the simulation, these differences somewhat even out towards the end of the acceleration process. While ionization injection in these simulations shows a larger pointing jitter, the results are of the same order of magnitude. It should be noted that in these simulations we forced the pulse asymmetry from the beginning by using pulses with a short upramp. In the experiment, the pulse initially had a long upramp, with single cycle in a steep pulse front developing only after significant propagation through the plasma.

To highlight the relevance of the pulse front steepness for the beam pointing jitter, we show in Fig. 14 a PIC simulation result for the beam pointing fluctuations for an initially Gaussian pulse shape with, e.g., equally long pulse rising and falling edges with a FWHM of $c\tau = 8$ μm. It demonstrates that the instability of the electron beam pointing occurs for typical LWFA pulse parameters and longer initial pulses after some propagation through the plasma once the pulse has sufficient time to self-steepen.

APPENDIX C: ADDITIONAL DETAILS ON THE BETATRON-BCO-RESONANCE MODEL

In Fig. 15, we show the dependence on the injection not being instantaneous, i.e., a distribution of t_i. Here, the injection point is varied uniformly over 0.5 BCO wavelengths. The jitter due to BCO resonance is still observable as in Fig. 8. The main effect of a long injection time is that the BCO leads to an additional beam emittance growth, as was discussed for instance in Refs. [28,39]. The larger beam emittance can be inferred in the figure from the wider distribution of the individual electron trajectories around their respective centroids compared to Fig. 8.

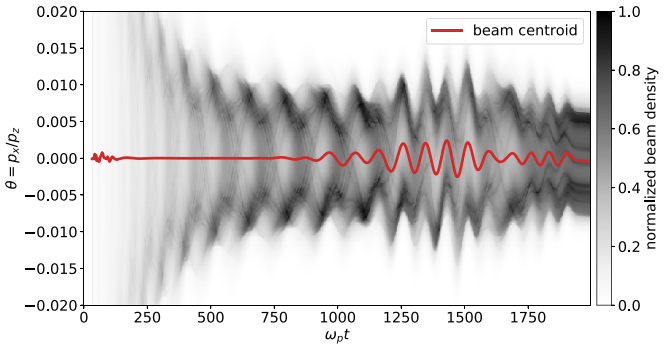

FIG. 14. Results of a PIC simulation with a temporally Gaussian pulse with an initial duration of $c\tau = 8$ μm and $a_0 = 4$ showing that the beam centroid starts oscillating eventually also for initially Gaussian pulses. The plot exhibits the density of the externally injected beam as a function of the pointing angle. After an initial phase where the beam centroid pointing (red curve) is stable at $\theta = 0$, the pointing jitter grows rapidly once the front edge has steepened, exciting bubble centroid oscillations resulting in large the beam centroid oscillation due to forced collective betatron oscillations when resonance is reached.

Figure 16 shows results for the polarization-dependent contribution $\Delta\theta = \sigma_P$ to the electron beam pointing jitter according to our betatron-BCO-resonance model, as presented in Eq. (5). It should be emphasized again that these model calculations are in qualitative agreement with the PIC simulation results shown in Fig. 10, despite the fact that in the model the BCO amplitude is treated as constant assuming a nonevolving laser pulse. Of course, one could alternatively model the BCO amplitude (and frequency) as time dependent as well, e.g., with input from PIC simulations, in order to obtain even better agreement.

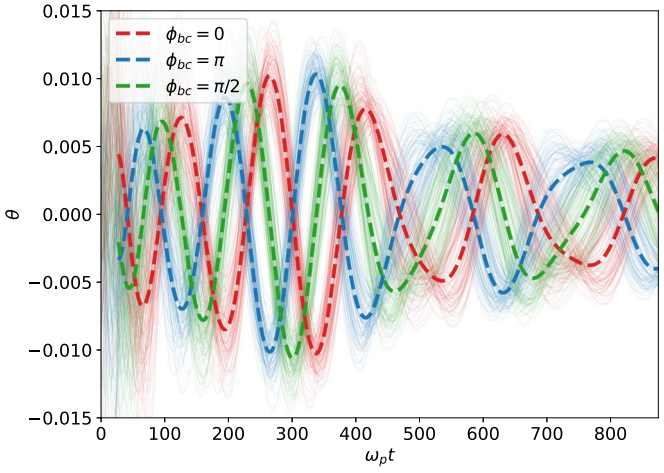

FIG. 15. Excitation of collective betatron oscillations with the injection point varied uniformly over 0.5 BCO wavelengths (compare with Fig. 8). The shot-to-shot pointing jitter due to BCO resonance is still present. In addition, the nonlocalized injection leads to an increased beam divergence as seen by the larger fluctuations of the electron orbits around their respective beam centroids.

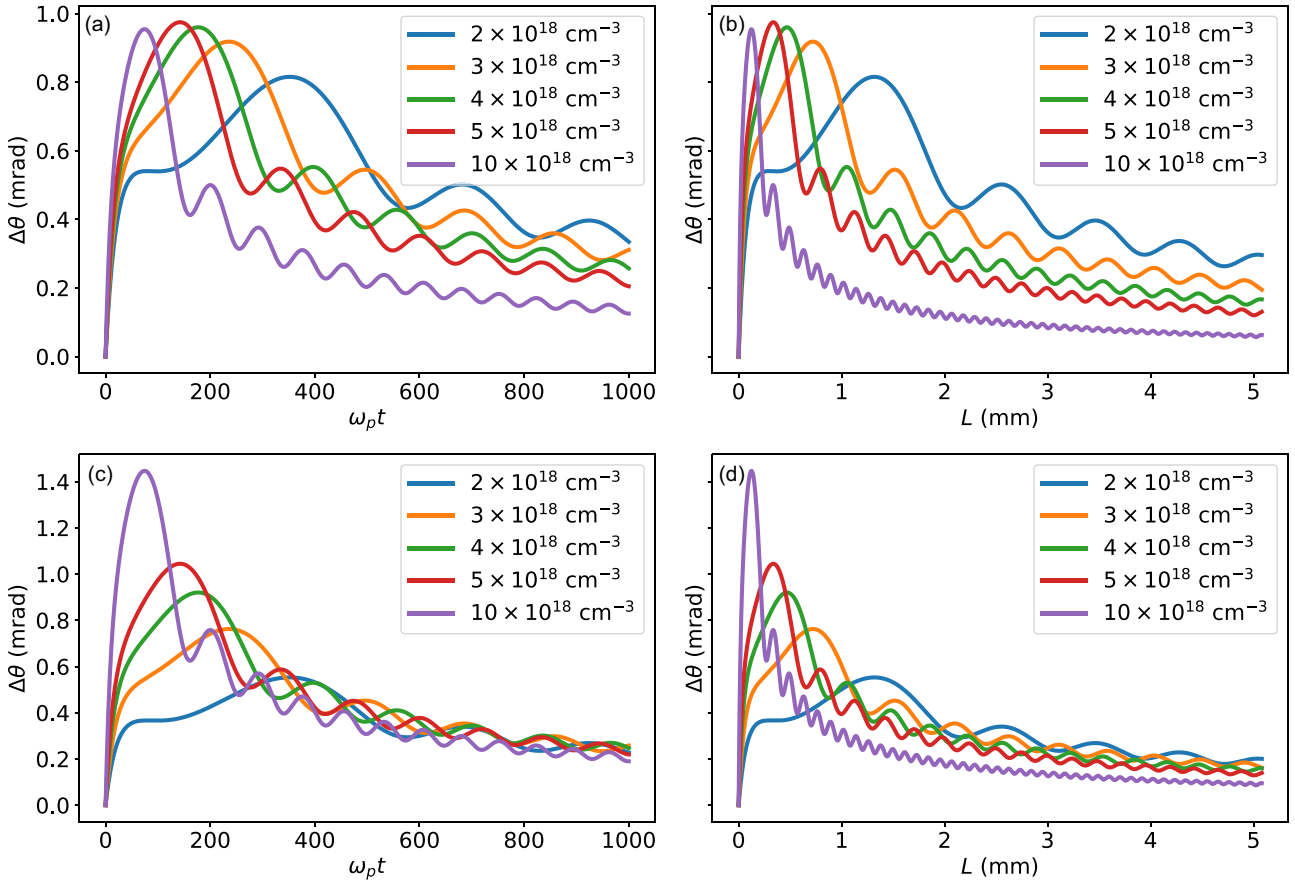

FIG. 16. Plot of the analytic result of the pointing jitter as given by Eq. (6). Results are shown for fixed $a_{\rm bc} = 0.005$ at various plasma densities (top panels) and for the bubble centroid oscillation amplitude scaling with density $a_{\rm bc} = 0.1/\gamma_p$ (lower panels). For convenience, we show the results both as a function of normalized $\omega_p t$ (left panels), as well as a function of the acceleration length in millimeters (right panels). All results show a fast initial increase of pointing jitter due to the betatron-BCO resonance before the $\Delta\theta = \sigma_P$ slowly decreases as the electrons are further accelerated and the betatron frequency drops as $\omega_\beta(t) \propto 1/\sqrt{2\gamma(t)}$.

[1] T. Tajima and J. M. Dawson, Laser electron accelerator, Phys. Rev. Lett. **43**, 267 (1979).

[2] O. Lundh, J. Lim, C. Rechatin, L. Ammoura, A. Ben-Ismaïl, X. Davoine, G. Gallot, J.-P. Goddet, E. Lefebvre, V. Malka *et al.*, Few femtosecond, few kiloampere electron bunch produced by a laser–plasma accelerator, Nat. Phys. **7**, 219 (2011).

[3] A. Buck, M. Nicolai, K. Schmid, C. Sears, A. Sävert, J. M. Mikhailova, F. Krausz, M. C. Kaluza, and L. Veisz, Real-time observation of laser-driven electron acceleration, Nat. Phys. **7**, 543 (2011).

[4] O. Zarini, J. C. Cabadağ, Y.-Y. Chang, A. Köhler, T. Kurz, S. Schöbel, W. Seidel, M. Bussmann, U. Schramm, A. Irman, and A. Debus, Multioctave high-dynamic range optical spectrometer for single-pulse, longitudinal characterization of ultrashort electron bunches, Phys. Rev. Accel. Beams **25**, 012801 (2022).

[5] J. Couperus, R. Pausch, A. Köhler, O. Zarini, J. Krämer, M. Garten, A. Huebl, R. Gebhardt, U. Helbig, S. Bock *et al.*, Demonstration of a beam loaded nanocoulomb-class laser wakefield accelerator, Nat. Commun. **8**, 487 (2017).

[6] S. K. Barber, J. van Tilborg, C. B. Schroeder, R. Lehe, H.-E. Tsai, K. K. Swanson, S. Steinke, K. Nakamura, C. G. R. Geddes, C. Benedetti, E. Esarey, and W. P. Leemans, Measured emittance dependence on the injection method in laser plasma accelerators, Phys. Rev. Lett. **119**, 104801 (2017).

[7] A. J. Gonsalves, K. Nakamura, J. Daniels, C. Benedetti, C. Pieronek, T. C. H. de Raadt, S. Steinke, J. H. Bin, S. S. Bulanov, J. van Tilborg, C. G. R. Geddes, C. B. Schroeder, C. Tóth, E. Esarey, K. Swanson, L. Fan-Chiang, G. Bagdasarov, N. Bobrova, V. Gasilov, G. Korn *et al.*, Petawatt laser guiding and electron beam acceleration to 8 GeV in a laser-heated capillary discharge waveguide, Phys. Rev. Lett. **122**, 084801 (2019).

[8] E. Esarey, C. B. Schroeder, and W. P. Leemans, Physics of laser-driven plasma-based electron accelerators, Rev. Mod. Phys. **81**, 1229 (2009).

[9] T.-Y. Chien, C.-L. Chang, C.-H. Lee, J.-Y. Lin, J. Wang, and S.-Y. Chen, Spatially localized self-injection of electrons in a self-modulated laser-wakefield accelerator by using a laser-induced transient density ramp, Phys. Rev. Lett. **94**, 115003 (2005).

[10] J. Faure, C. Rechatin, A. Norlin, A. Lifschitz, Y. Glinec, and V. Malka, Controlled injection and acceleration of electrons in plasma wakefields by colliding laser pulses, Nature (London) **444**, 737 (2006).

[11] A. Pak, K. A. Marsh, S. F. Martins, W. Lu, W. B. Mori, and C. Joshi, Injection and trapping of tunnel-ionized electrons into laser-produced wakes, Phys. Rev. Lett. **104**, 025003 (2010).

[12] C. McGuffey, A. G. R. Thomas, W. Schumaker, T. Matsuoka, V. Chvykov, F. J. Dollar, G. Kalintchenko, V. Yanovsky, A. Maksimchuk, K. Krushelnick, V. Y. Bychenkov, I. V. Glazyrin, and A. V. Karpeev, Ionization induced trapping in a laser wakefield accelerator, Phys. Rev. Lett. **104**, 025004 (2010).

[13] J. M. Cole, K. T. Behm, E. Gerstmayr, T. G. Blackburn, J. C. Wood, C. D. Baird, M. J. Duff, C. Harvey, A. Ilderton, A. S. Joglekar, K. Krushelnick, S. Kuschel, M. Marklund, P. McKenna, C. D. Murphy, K. Poder, C. P. Ridgers, G. M. Samarin, G. Sarri, D. R. Symes *et al.*, Experimental evidence of radiation reaction in the collision of a high-intensity laser pulse with a laser-wakefield accelerated electron beam, Phys. Rev. X **8**, 011020 (2018).

[14] K. Poder, M. Tamburini, G. Sarri, A. Di Piazza, S. Kuschel, C. D. Baird, K. Behm, S. Bohlen, J. M. Cole, D. J. Corvan, M. Duff, E. Gerstmayr, C. H. Keitel, K. Krushelnick, S. P. D. Mangles, P. McKenna, C. D. Murphy, Z. Najmudin, C. P. Ridgers, G. M. Samarin *et al.*, Experimental signatures of the quantum nature of radiation reaction in the field of an ultraintense laser, Phys. Rev. X **8**, 031004 (2018).

[15] A. Fedotov, A. Ilderton, F. Karbstein, B. King, D. Seipt, H. Taya, and G. Torgrimsson, Advances in QED with intense background fields Phys. Rep. **1010**, 1 (2023).

[16] K. Nakamura, H.-S. Mao, A. J. Gonsalves, H. Vincenti, D. E. Mittelberger, J. Daniels, A. Magana, C. Toth, and W. P. Leemans, Diagnostics, control and performance parameters for the BELLA high repetition rate petawatt class laser, IEEE J. Quantum Electron. **53**, 1 (2017).

[17] A. Gonsalves, K. Nakamura, J. Daniels, H.-S. Mao, C. Benedetti, C. Schroeder, C. Tóth, J. Van Tilborg, D. Mittelberger, S. Bulanov *et al.*, Generation and pointing stabilization of multi-GeV electron beams from a laser plasma accelerator driven in a pre-formed plasma waveguide, Phys. Plasmas **22**, 056703 (2015).

[18] Y. Ma, D. Seipt, S. Dann, M. Streeter, C. Palmer, L. Willingale, and A. Thomas, Angular streaking of betatron x-rays in a transverse density gradient laser-wakefield accelerator, Phys. Plasmas **25**, 113105 (2018).

[19] S. Kuschel, M. B. Schwab, M. Yeung, D. Hollatz, A. Seidel, W. Ziegler, A. Sävert, M. C. Kaluza, and M. Zepf, Controlling the self-injection threshold in laser wakefield accelerators, Phys. Rev. Lett. **121**, 154801 (2018).

[20] A. Popp, J. Vieira, J. Osterhoff, Z. Major, R. Hörlein, M. Fuchs, R. Weingartner, T. P. Rowlands-Rees, M. Marti, R. A. Fonseca, S. F. Martins, L. O. Silva, S. M. Hooker, F. Krausz, F. Grüner, and S. Karsch, All-optical steering of laser-wakefield-accelerated electron beams, Phys. Rev. Lett. **105**, 215001 (2010).

[21] M. Schnell, A. Sävert, I. Uschmann, M. Reuter, M. Nicolai, T. Kämpfer, B. Landgraf, O. Jäckel, O. Jansen, A. Pukhov *et al.*, Optical control of hard x-ray polarization by electron injection in a laser wakefield accelerator, Nat. Commun. **4**, 2421 (2013).

[22] S. Lee, T. H. Lee, D. N. Gupta, H. S. Uhm, and H. Suk, Enhanced betatron oscillations in laser wakefield acceleration by off-axis laser alignment to a capillary plasma waveguide, Plasma Phys. Control. Fusion **57**, 075002 (2015).

[23] K. Huang, Y. Li, D. Li, L. Chen, M. Tao, Y. Ma, J. Zhao, M. Li, M. Chen, M. Mirzaie *et al.*, Resonantly enhanced betatron hard x-rays from ionization injected electrons in a laser plasma accelerator, Sci. Rep. **6**, 27633 (2016).

[24] A. F. Lifschitz and V. Malka, Optical phase effects in electron wakefield acceleration using few-cycle laser pulses, New J. Phys. **14**, 053045 (2012).

[25] D. Guénot, D. Gustas, A. Vernier, B. Beaurepaire, F. Böhle, M. Bocoum, M. Lozano, A. Jullien, R. Lopez-Martens, A. Lifschitz, and J. Faure, Relativistic electron beams driven by kHz single-cycle light pulses, Nat. Photon. **11**, 293 (2017).

[26] J. Faure, D. Gustas, D. Guénot, A. Vernier, F. Böhle, M. Ouillé, S. Haessler, R. Lopez-Martens, and A. Lifschitz, A review of recent progress on laser-plasma acceleration at kHz repetition rate, Plasma Phys. Control. Fusion **61**, 014012 (2019).

[27] R. Polanek, N. A. M. Hafz, Z. Lécz, D. Papp, C. Kamperidis, S. Brunner, E. R. Szabó, T. Tőkés, and K. Hideghéty, 1 kHz laser accelerated electron beam feasible for radiotherapy uses: A PIC–Monte Carlo based study, Nucl. Instrum. Methods Phys. Res. Sect. A **987**, 164841 (2021).

[28] J. Huijts, I. A. Andriyash, L. Rovige, A. Vernier, and J. Faure, Identifying observable carrier-envelope phase effects in laser wakefield acceleration with near-single-cycle pulses, Phys. Plasmas **28**, 043101 (2021).

[29] F. Salehi, M. Le, L. Railing, M. Kolesik, and H. M. Milchberg, Laser-accelerated, low-divergence 15-MeV quasimonoenergetic electron bunches at 1 kHz, Phys. Rev. X **11**, 021055 (2021).

[30] J. Huijts, L. Rovige, I. A. Andriyash, A. Vernier, M. Ouillé, J. Kaur, Z. Cheng, R. Lopez-Martens, and J. Faure, Waveform control of relativistic electron dynamics in laser-plasma acceleration, Phys. Rev. X **12**, 011036 (2022).

[31] T. Kurz, J. P. Couperus, J. M. Krämer, H. Ding, S. Kuschel, A. Köhler, O. Zarini, D. Hollatz, D. Schinkel, R. D'Arcy *et al.*, Calibration and cross-laboratory implementation of scintillating screens for electron bunch charge determination, Rev. Sci. Instrum. **89**, 093303 (2018).

[32] W. Lu, M. Tzoufras, C. Joshi, F. S. Tsung, W. B. Mori, J. Vieira, R. A. Fonseca, and L. O. Silva, Generating multi-GeV electron bunches using single stage laser wakefield acceleration in a 3D nonlinear regime, Phys. Rev. ST Accel. Beams **10**, 061301 (2007).

[33] J. Ferri and X. Davoine, Enhancement of betatron x rays through asymmetric laser wakefield generated in transverse density gradients, Phys. Rev. Accel. Beams **21**, 091302 (2018).

[34] For the analysis of the electron pointing jitter measurements, the method of bootstrapping was employed. Hereby, the position of each shot in a dataset set represents a sample. By bootstrapping, we refer to resampling the measured distribution with replacement and the same size as the original sample size. Repeating this process many times and calculating the mean of each resampled distribution leads to a histogram of the distribution of mean values. The mean and the variance of this histogram represent the mean and variance of the mean of the pointing jitter of the initial sample of the

experimentally measured pointing position distribution of the electrons.

[35] Y. Ma, D. Seipt, A. E. Hussein, S. Hakimi, N. F. Beier, S. B. Hansen, J. Hinojosa, A. Maksimchuk, J. Nees, K. Krushelnick, A. G. R. Thomas, and F. Dollar, Polarization-dependent self-injection by above threshold ionization heating in a laser wakefield accelerator, Phys. Rev. Lett. **124**, 114801 (2020).

[36] Y. Ma, D. Seipt, A. E. Hussein, S. Hakimi, N. F. Beier, S. B. Hansen, J. Hinojosa, A. Maksimchuk, J. Nees, K. Krushelnick, A. G. R. Thomas, and F. Dollar, The effects of laser polarization and wavelength on injection dynamics of a laser wakefield accelerator, Phys. Plasmas **28**, 063101 (2021).

[37] J. Kim, T. Wang, V. Khudik, and G. Shvets, Subfemtosecond wakefield injector and accelerator based on an undulating plasma bubble controlled by a laser phase, Phys. Rev. Lett. **127**, 164801 (2021).

[38] J. Kim, T. Wang, V. Khudik, and G. Shvets, Polarization control of electron injection and acceleration in the plasma by a self steepening laser pulse, New J. Phys. **25**, 033009 (2023).

[39] E. N. Nerush and I. Y. Kostyukov, Carrier-envelope phase effects in plasma-based electron acceleration with few-cycle laser pulses, Phys. Rev. Lett. **103**, 035001 (2009).

[40] C. D. Decker, W. B. Mori, K. Tzeng, and T. Katsouleas, The evolution of ultra-intense, short-pulse lasers in underdense plasmas, Phys. Plasmas **3**, 2047 (1996).

[41] J. Schreiber, C. Bellei, S. P. D. Mangles, C. Kamperidis, S. Kneip, S. R. Nagel, C. A. J. Palmer, P. P. Rajeev, M. J. V. Streeter, and Z. Najmudin, Complete temporal characterization of asymmetric pulse compression in a laser wakefield, Phys. Rev. Lett. **105**, 235003 (2010).

[42] Y. Ma, L. Chen, D. Li, W. Yan, K. Huang, M. Chen, Z. Sheng, K. Nakajima, T. Tajima, and J. Zhang, Generation of femtosecond γ-ray bursts stimulated by laser-driven hosing evolution, Sci. Rep. **6**, 30491 (2016).

[43] M. J. V. Streeter, S. Kneip, M. S. Bloom, R. A. Bendoyro, O. Chekhlov, A. E. Dangor, A. Döpp, C. J. Hooker, J. Holloway, J. Jiang, N. C. Lopes, H. Nakamura, P. A. Norreys, C. A. J. Palmer, P. P. Rajeev, J. Schreiber, D. R. Symes, M. Wing, S. P. D. Mangles, and Z. Najmudin, Observation of laser power amplification in a self-injecting laser wakefield accelerator, Phys. Rev. Lett. **120**, 254801 (2018).

[44] T. J. Mehrling, R. A. Fonseca, A. Martinez de la Ossa, and J. Vieira, Mitigation of the hose instability in plasma-wakefield accelerators, Phys. Rev. Lett. **118**, 174801 (2017).

[45] C. M. Bender and S. A. Orszag, *Advanced Mathematical Methods for Scientists and Engineers I* (Springer, New York, 1999).

[46] M. Kirchen, S. Jalas, P. Messner, P. Winkler, T. Eichner, L. Hübner, T. Hülsenbusch, L. Jeppe, T. Parikh, M. Schnepp, and A. R. Maier, Optimal beam loading in a laser-plasma accelerator, Phys. Rev. Lett. **126**, 174801 (2021).

[47] A. Golinelli, X. Chen, B. Bussière, E. Gontier, P.-M. Paul, O. Tcherbakoff, P. D'Oliveira, and J.-F. Hergott, CEP-stabilized, sub-18 fs, 10 khz and TW-class 1 khz dual output Ti:Sa laser with wavelength tunability option, Opt. Express **27**, 13624 (2019).

[48] http://www.gauss-centre.eu.

[49] J. Derouillat, A. Beck, F. Pérez, T. Vinci, M. Chiaramello, A. Grassi, M. Flé, G. Bouchard, I. Plotnikov, N. Aunai, J. Dargent, C. Riconda, and M. Grech, SMILEI: A collaborative, open-source, multi-purpose particle-in-cell code for plasma simulation, Comput. Phys. Commun. **222**, 351 (2018).

[50] D. Foreman-Mackey, D. W. Hogg, D. Lang, and J. Goodman, emcee: The MCMC hammer, Publ. Astron. Soc. Pac. **125**, 306 (2013).